Contents lists available at ScienceDirect

Materials Characterization

journal homepage: www.elsevier.com

Lower-bound dislocation density mapping in microcoined tantalum using high-resolution electron backscatter diffraction

Greg C. Randall [a,*], Kameron R. Hansen [b], Brian Jackson [b], David T. Fullwood [b]

[a] General Atomics, 3550 General Atomics Ct., San Diego, CA 92121, United States of America
[b] Brigham Young University, Provo, UT 84602, United States of America

ARTICLE INFO

Keywords:
Dislocation density
EBSD
Metals
Microstructure formation
Microforming
Coining

ABSTRACT

High-resolution electron backscatter diffraction (HR-EBSD) is used to map the geometrically necessary dislocation (GND) density in the cross-sections of annealed, rolled, and microcoined tantalum foils that are typical targets used in modern laser-induced compression materials science studies. The microcoined samples are characteristic of microforming, where the deformation length scale is on the order of the grain size (~50 μm). In particular, inhomogeneities in dislocation density maps across 0.1–1 mm regions of interest are compared with expectations from slip line field approximations. The average HR-EBSD GND dislocation density measurements in various annealed and cold worked tantalum samples are compared with corresponding dislocation density approximations from microhardness measurements. GND densities in the range $10^{13} - 10^{15}$ m^{-2} are typical.

1. Introduction

Dislocations, or linear defects in a crystal lattice, are at the heart of a metal's mechanical behavior [1–3]. Plastic deformation requires generation and movement of dislocations in order to maintain continuity or compatibility [4]. Typically these structures are stored in regions of high strain and are oriented based on the metal's crystal structure and applied deformation geometry. Dislocations often assemble into non-uniform structures such as cells, tangles, or bands [1].

Dislocation inhomogeneities are key to the function and understanding of metals, for example, in the areas of fracture, formability, wear, corrosion and fatigue. They are particularly important in modern plasticity analysis that probes metal strength at extreme length and time scales. For example, in the relatively new field of microforming [5], the deformation scale shrinks to the grain size or even smaller, resulting in length scale-dependent strength. Studies of nano- and micro-scale indentation have shown length-scale dependent hardness and spatially non-uniform dislocation structures [6–16]. Furthermore, in the field of High Energy Density (HED) materials science where materials are studied at extremely high strain rates ($>10^7$ s^{-1}) [17], dislocation density is an input parameter in a multiscale deformation model [18,19]. The HED multiscale deformation models are typically tested in laser compression experiments in which microrippled metal targets are observed during a laser-generated high strain rate compression wave [20]. Strength can become independent of the initial dislocation microstructure at high strain rates [19,20]. However, current research at even higher pressure and strain rate suggests strength sensitive to the initial dislocation microstructure, presumably due to precursor wave effects [19]. Due to the fabrication process, it is expected that the dislocation density in these targets is non-uniform and much higher than in the native raw material. Dislocation density has previously been approximated at points of these laser targets [20], but not mapped.

Dislocations can be observed in several ways [1]. The most well-known traditional method is TEM (transmission electron microscopy) in which dislocations are directly imaged at high-resolution and high-magnification in a small (typically $<$μm) region of a very thin sample. However, TEM is limited by difficult preparation and a very small region of observation. An alternate way to image dislocations, called electron channelling contrast imaging (ECCI), allows for larger regions of interest, albeit at lower resolution so that dislocation images saturate in typical cold-worked samples [8,21,22]. As opposed to directly imaging dislocations, indirect dislocation mapping methods have also been developed by treating dislocations from a continuum viewpoint and using electron backscatter diffraction (EBSD) to relate crystal misorientation measurements to the presence of a subset of dislocations called geometrically necessary dislocations (GNDs) [14,23–27]. These GND dislocations are the dislocations that are required for compatibility as a

* Corresponding author.
Email address: randall@fusion.gat.com (G.C. Randall)

https://doi.org/10.1016/j.matchar.2019.04.033
Received 31 January 2019; Received in revised form 25 April 2019; Accepted 25 April 2019
Available online xxx

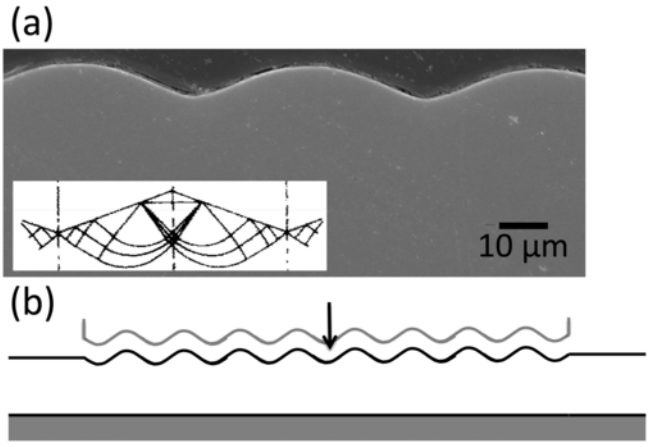

Fig. 1. (a) SEM cross-section of coined Ta and the expected slip line field at an intermediate stage [42]. (b) Schematic of microcoining.

Table 1
Tantalum samples.

Vendor	Deformation condition	Purity	Microhardness (*HV*)
Starck (NRC08)	Annealed	99.99%	87.9
Goodfellow (TA000490)	Annealed	99.9%	100.6
Goodfellow (TA002105)	Single crystal (100)	99.999%	75.2
ESPI (KND3899)	Annealed	99.99%	80.7
ESPI (49931)	As-rolled	99.99%	125.7

crystalline material plastically deforms [28]. The remaining dislocations, termed statistically stored dislocations (SSDs), can be envisioned as dislocations that cause locally offsetting misorientations so that they do not contribute to a long-range misorientation in the crystal structure. In a discrete lattice picture at atomic length scales, all dislocations are technically GNDs, however as the length scale of observation grows the dislocation population can be envisioned as those that are necessary for compatibility (GNDs) and those that locally offset each other (SSDs) so that $\rho_d = \rho_{GND} + \rho_{SSD}$. The resolution and step size of an EBSD scan, in comparison to the deformation or dislocation structure length scale, will therefore determine the range of GND dislocation content that can be measured. The most sophisticated method to date is known as high resolution EBSD (HR-EBSD) since it uses algorithms that determine crystal orientation differences to extremely high resolution, with discernible misorientations of 0.005° [29].

The HR-EBSD method has recently been used to map GND density and strain for various applications. For example, HR-EBSD was used to study Ni grain fragmentation in microextrusion, where the inhomogeneous dislocation density within the initial grains was found to correspond to grain refinement [30]. Several have used HR-EBSD to map the dislocations in nano- and micro-indentation fields [6–16]. Considering the small deformation scale and high local strain gradients, the GND content is generally dominant on the EBSD step-size scale and ignoring the SSD content would lead to O[1] reduction of the characterized dislocation density compared to the actual ρ_d ("O": order) [13,31,32]. HR-EBSD showed the GND dislocation density can be highly non-uniform with bands of concentrated dislocations underneath the indenter [7,10–12,15,16].

Although several researchers have used simulated dislocation fields to verify the HR-EBSD algorithms and GND/SSD statistics [13,33,34], only limited work has been performed to validate the HR-EBSD measurements in experimental samples. GND measurements (without the HR-EBSD image analysis algorithms) in 10% compressed Cu were 15–30% of ρ_d reported from similar studies by TEM and neutron scattering [35]. Averaged GNDs from 3D HR-EBSD on a bent ion-milled Cu microcantilever were 1.5× higher than an analytically predictable ρ_{GND} [36]. Comparisons of GND from HR-EBSD have been made to ρ_d from ECCI [8,37–39] and measurements were similar as long as $\rho_d < 10^{14}$ m^{-2} (above which ECCI dislocations are hard to resolve).

In this study, we use HR-EBSD to map and compare the GND dislocation density (ρ_{GND}) in microformed rippled tantalum foils (a typical target for HED laser compression materials science studies) and the annealed raw material. This is the first incorporation of a dislocation mapping method for small-scale laser targets used to probe extreme de-

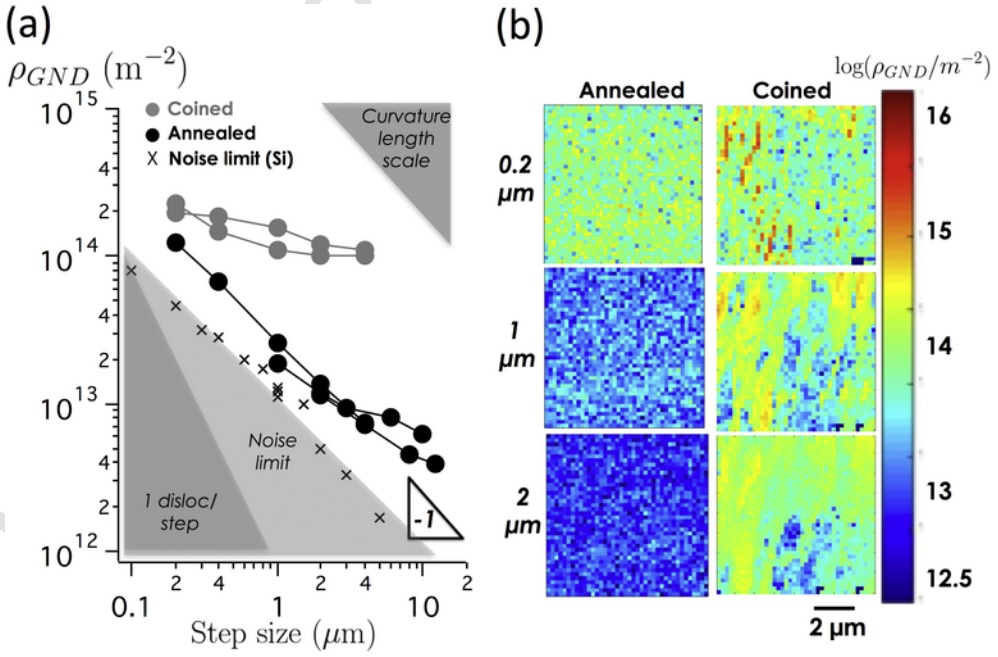

Fig. 2. (a) Effect of HR-EBSD step size on the GND dislocation density for coined (gray, in a surface region ~λ deep) and annealed (black) Ta. The noise threshold for our system is plotted using results from Si wafer scans. (b) Detailed views of small area scans at different effectively sampled step sizes on annealed and coined Ta.

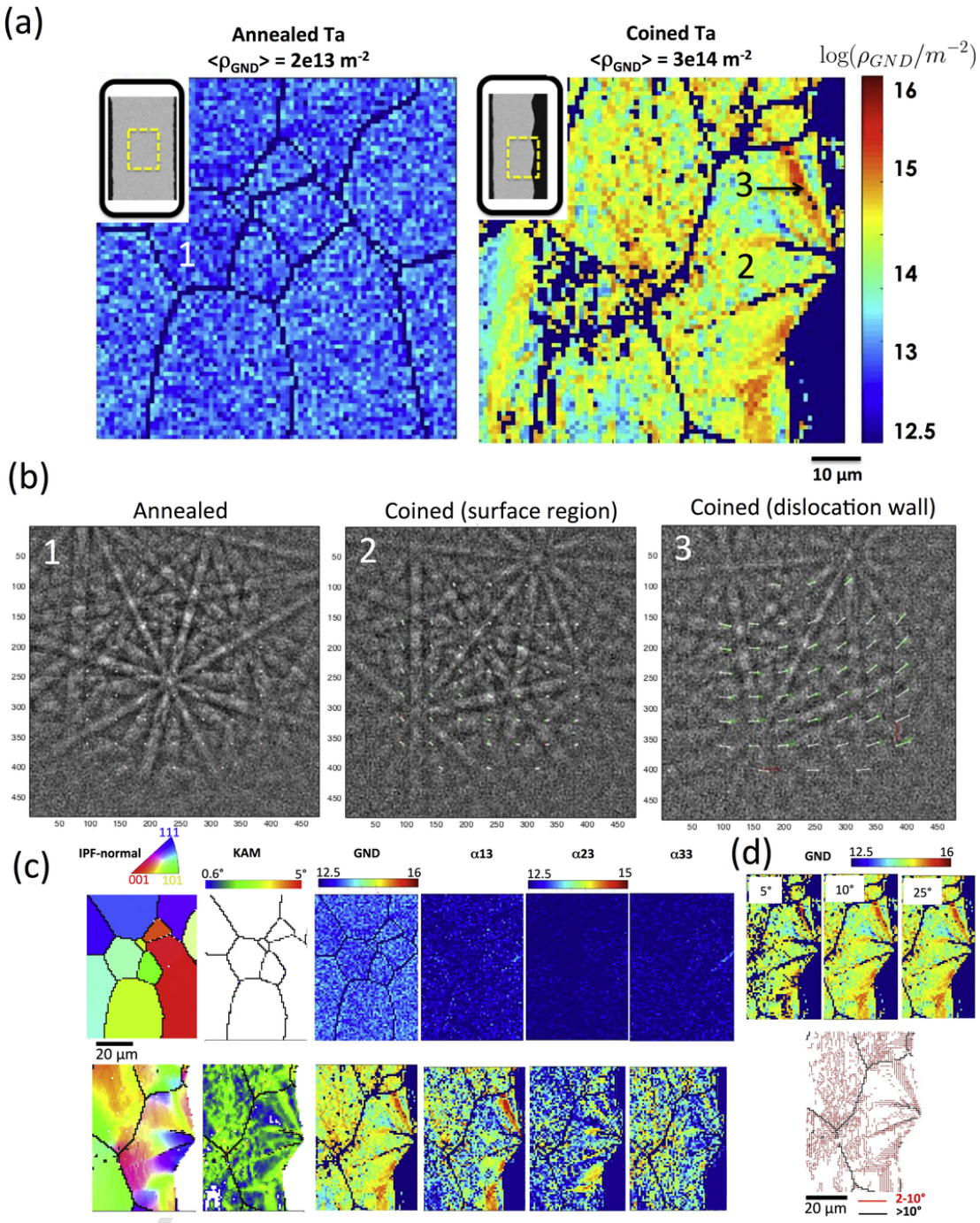

Fig. 3. (a) GND dislocation density maps for cross-sections of annealed Starck Ta (left) and the same material coined with surface ripples (right). (b) Sample Kikuchi diffraction patterns (with locations indicated in maps above) with computed HR-EBSD shift vector fields (**q**) plotted. (c) Inverse pole figures (IPF) normal to the ripple surface, kernel average misoritentaion (KAM) and the HR-EBSD detailed GND maps (total and α_{i3} components). (d) GND maps for coined Ta for increasing OpenXY misorientation cut-off (5–25°) and orientation boundary map for the coined Ta sample (2–10° in red, >10° in black). (For interpretation of the references to color in this figure legend, the reader is referred to the web version of this article.)

formation conditions and continues the application of HR-EBSD to microforming plasticity beyond single indents to a high-strain, non-stationary slip field. Average ρ_{GND} values are compared to simple predictions from strain gradient plasticity and characteristics of the expected slip line field to explain non-homogeneous GND results. We evaluate the effect of step size on the HR-EBSD results. Furthermore, to corroborate these HR-EBSD results, we compare average ρ_{GND} measurements to ρ_d measurements correlated from microhardness measurements in Ta samples in various states of deformation.

2. Analytical methods

Before reviewing the analytical methods used to evaluate GND dislocation generation, we first briefly review the microcoining process with details on engineering [40] and mechanics [41] found elsewhere. Fig. 1(a) shows a typical ripple cross-section along with a slip line field for closed die coining from Ref. [42]. Fig. 1(b) shows the die configuration used to form a ripple. These rippled foils are O[mm] on a lateral scale and we study two characteristic thickness ranges: ~100 μm and

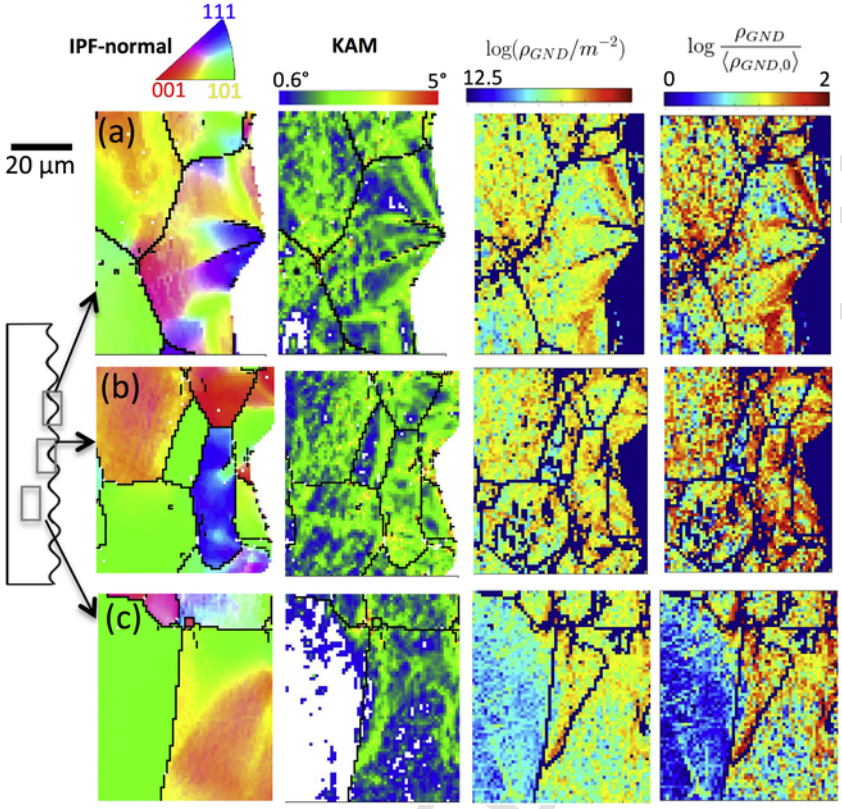

Fig. 4. Maps in different regions of a coined 0.1 mm thick Starck Ta sample with a A = 5 μm, λ = 50 μm ripple. Locations are (a) centered at a ripple peak, (b) centered at a ripple valley, and (c) centered 40 ± 10 μm below the ripple mid plane. From left to right: Inverse Pole Figure (IPF) normal to the ripple surface, kernal average misorientation (KAM), HR-EBSD GND dislocation density, and HR-EBSD GND dislocation density scaled by the average GND dislocation density in the Ta raw material before coining.

~1000 μm. Microcoining can be distinguished from standard coining because 1) the deformation scale is on the order or smaller than the grain size and 2) alternative plasticity fields exist depending on the workpiece thickness (as discussed in Ref. [41]). The plasticity would be effectively closed die inverse extrusion for thin foils (under 150 μm here) with a characteristic large forming load and an elastic-plastic boundary within the workpiece cross-section. The plasticity would be open die upsetting with a lower forming load and thru-thickness plasticity at large thickness (above 500 μm here). We would expect both the grain size and plasticity geometry to lead to non-homogeneous dislocation generation at multiple scales during the pattern formation.

2.1. HR-EBSD

HR-EBSD can map GND dislocation density from an electron backscatter diffraction (EBSD) scan using cross-correlation diffraction pattern image analysis along with calculations and assumptions from a continuum model of dislocations. This paper does not advance the calculation method, continuum model, and image analysis machinery of HR-EBSD so the HR-EBSD background is streamlined with referrals to appropriate papers [10,11,16,24,43,44].

Dislocation density is typically defined in terms of the line length of dislocations in a given crystal volume, obtained by summing over dislocations in all possible slip systems of a material [4]. In a continuum view of dislocations [4,28,45–50], a geometrically necessary dislocation density tensor α can be written in terms of gradients of an elastic distortion tensor β_e: $\alpha = \times \beta_e$. The elastic distortion captures both the lattice elastic strain and its rotation. An experimental EBSD scan gathers projected electron diffraction pattern images point-by-point across a smooth crystalline sample's surface [51–55]. These diffraction patterns, called Kikuchi patterns, are then used to construct a 2D lattice orientation map of the scanned surface, with a rotation axis and rotation angle measured at each point [56]. Extracting the orientation and/or distortion requires image analysis algorithms applied to the Kikuchi patterns. The most basic image analysis method uses a Hough transform to calculate absolute orientation from each Kikuchi pattern. The error from the Hough image analysis typically dominates once local misorientations are under 0.5–1° and limits the Hough algorithm to only detecting high dislocation densities $>10^{14}$ m^{-2} [57] (and only where elastic strain gradients are negligible). On the other hand, HR-EBSD uses cross-correlation image analysis to improve misorientation calculation by two orders of magnitude and determines β_e with both elastic strain and rotational components [29,57–59]. Specifically, it calculates shifts between two Kikuchi diffraction patterns taken from neighboring points. These shift vectors (**q**) are then related to the elastic distortion (rotation including elastic strain) by small strain elasticity and vector math. However, both HR-EBSD and Hough-based EBSD analysis are typically performed on a surface, so they cannot measure orientation gradients into the surface. Consequently, various components of α cannot be fully recovered [56]. Estimates of the overall density can be made from the L1 or L2 norm of α [4,9,11,16,60]. The L1 norm will be used in this work, as tested and described in Ref. [11].

2.2. Expected $\langle\rho_{GND}\rangle$ from strain gradient plasticity

Strain gradient plasticity models have been proposed to explain length-scale-dependent plasticity by assuming a uniform generation of GNDs on the local deformation length scale L: $\langle\rho_{GND}\rangle = 4\bar{\varepsilon}/(bL)$, where b is the Burger's vector length and $\bar{\varepsilon}$ is the strain [28]. Envisioning the plastic zone underneath the ripple $L = \lambda/2$ deep [41] as the strain gradient region of interest, a tantalum microcoined ripple with $b = 2.9 \times 10^{-10}$ m, $\lambda/2 = 25$ μm and $\bar{\varepsilon} = 0.1 - 0.5$ would expect to have $\langle\rho_{GND}\rangle \sim 0.5 - 3 \times 10^{14}$ m^{-2}. This is expected to depend on the

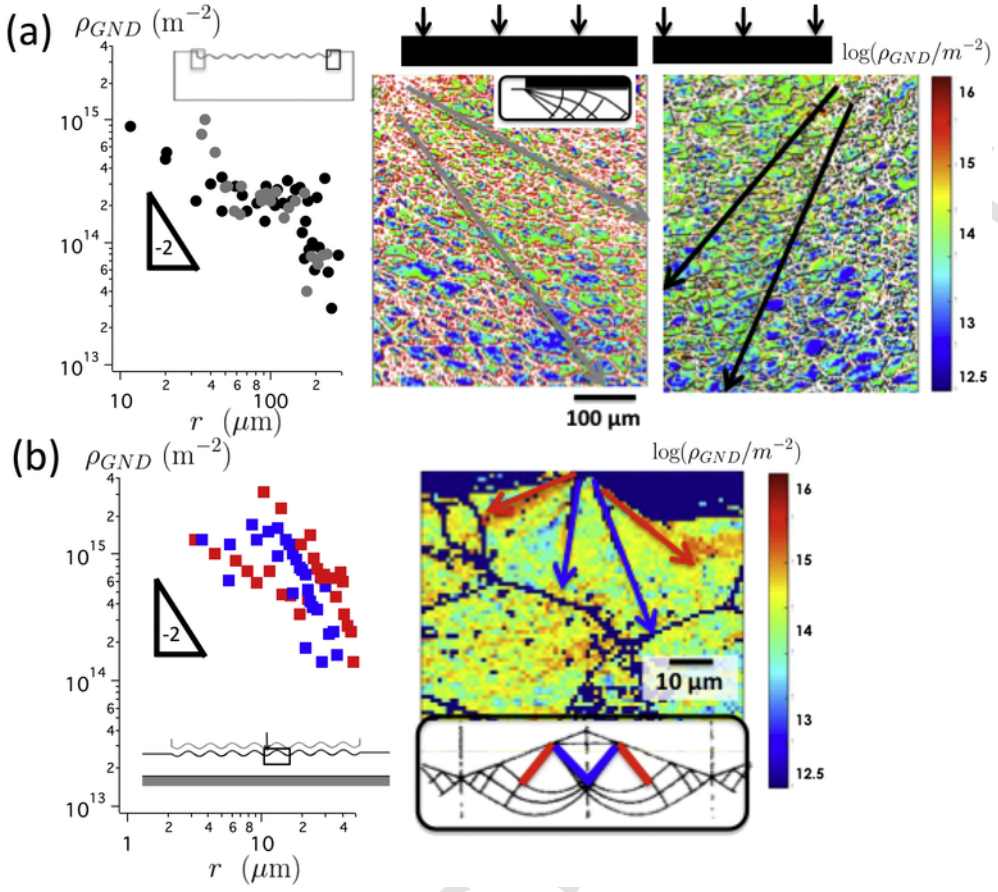

Fig. 5. GND dislocation density in regions of coined Ta expected to show centered fan slip behavior (as a function of distance from the fan center) (a) at either edge under an open die for 1-mm thick Ta (approximate die location indicated by black bar) and (b) at the peak of a coined ripple in 0.15-mm thick Ta.

representative strain for the coining process, which depends on the ripple amplitude A and pressing die geometry (open vs. closed) [41,42]. Note that strain gradient models are not very well-posed for bcc materials at low temperatures [61], however we do note that our microcoining process (and this study) is performed at 200°C to lower the Ta flow stress. Nevertheless, our analysis will compare with this simple scaling for map average GND dislocation density; based on the past work for indentation we expect the GND storage to be spatially non-uniform.

2.3. Expected ρ_{GND} from slip line fields

The predicted non-homogeneity of the GND distribution may be evaluated with a slip line field and some approximations. In a rigid-plastic material in plane strain, slip lines are lines tangent to surfaces of maximal tangential stress in a plastic flow field and maximum rate of shear strain. If a slip line field exists for a plastic deformation process, with a few additional approximations, they can be used to estimate the GND storage [62]. Assuming the rigid-ideally plastic crystal ideally slips in all directions, GND dislocations are stored when a slip gradient exists on a slip line or when slip occurs on a curved slip line. Slip line field examples have been presented for indentation [62,63] and for rippled wedge coining [42]. Centered fans are common components in both cases. For example, they are depicted in Fig. 1(a) as the pie-slice regions of the slip line field. For a plane strain indentation field, assuming no radial slip occurs in a slip line field centered fan, the number of GND dislocations stored in the fan should scale as $\rho_{GND} \sim 1/r^2$ where r is the radial distance from the center of the fan (center point of pie slice-shaped sector) [62], with dislocation pile-ups against the rigid regions occurring along the radial slip lines. A ripple coining slip line field is non-stationary, changing character as the ripples pattern deeper into the metal [42]. At early patterning stages, each tooth of the ripple acts as a solitary indenter. At intermediate stages, the stressed regions under each indenter move up the indenter face, begin to interact, and the centered fans from neighboring die peaks presumably collide (Fig. 1(a) shows this in progress). In the case that the die has friction, a region of dead metal exists under the die peak abutting another shear zone (similar to a centered fan). Assuming the bcc Ta has multiple slip planes available, an approximation inherent to slip line field models, we will test if dislocations stack up in these centered fan high-shear zones over the non-stationary deformation pathway, with $\rho_{GND} \sim 1/r^2$ fall-off from approximate final locations of these centered fans (the ripple peak and in the middle of the die face). Previous viscoplasticity experiments of closed die rib formation support this hypothesis of high strain in regions moving up the ripple towards the final contact point with the die [64].

3. Experimental methods

3.1. Raw materials

Table 1 lists the various tantalum samples used here, including vendor. Additionally, we coined ripples (amplitude $A = 5$ µm, wavelength $\lambda = 50$ µm) into a subset of these (thinned into 50–1000 µm thick foils) with nitrided steel dies as described elsewhere [40,41].

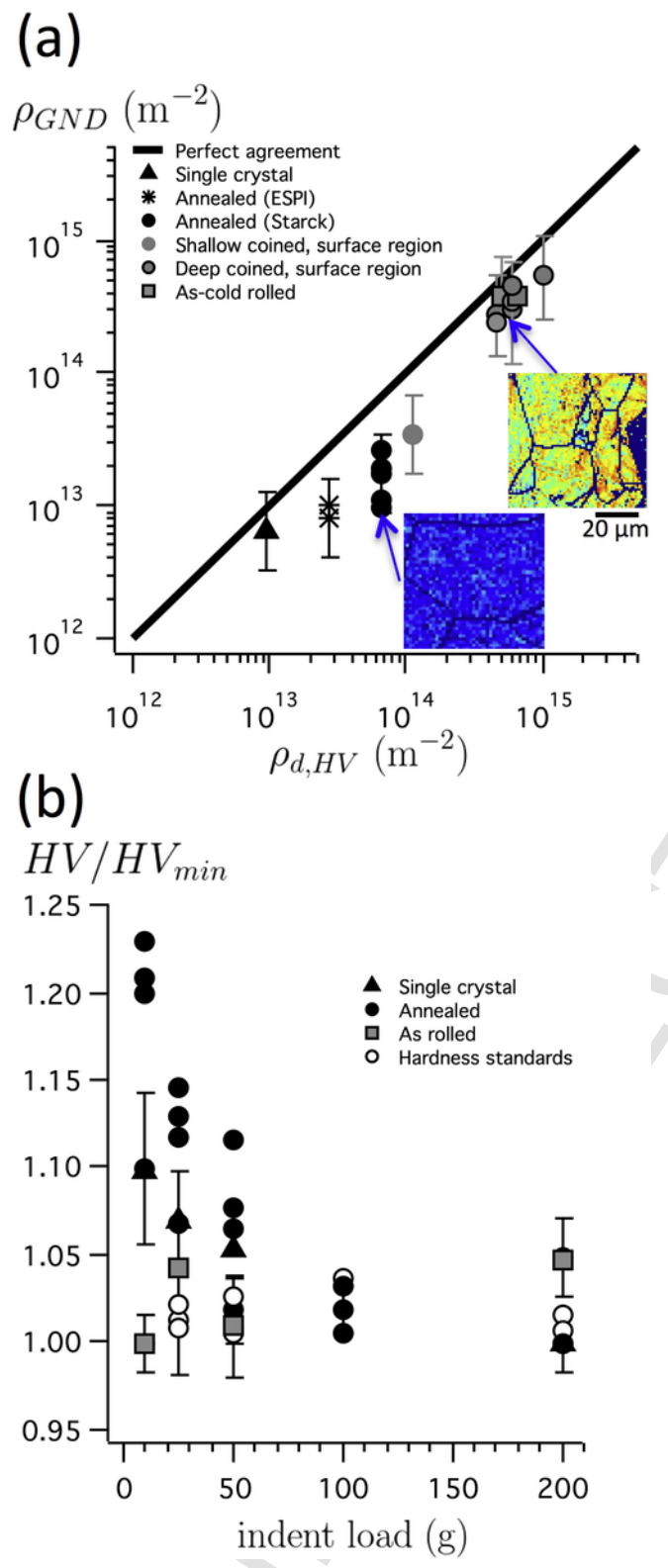

Fig. 6. (a) GND dislocation density determined from HR-EBSD as a function of dislocation density calculated from microhardness measurements for various Ta samples. (b) Effect of microhardness load on hardness reading.

3.2. EBSD scans

EBSD was performed on a JEOL JSM 6610 (JEOL USA, Peabody, MA) tungsten filament SEM with Aztec EBSD software (Oxford Instruments, Concord, MA) and a Nordlys-F fast detector (Oxford Instruments, 640 × 480 pixels). Scan settings were: 20 kV accelerating voltage, 70° tilt, 30 μm aperture at spot size 50 (~1 nA from vendor), a working distance of 13–14 mm, 1 × 1 camera pixel binning, 8-bit background-subtracted Kikuchi pattern images, 1000 ms exposure time, a camera-to-specimen distance of 18.6 mm, and Hough resolution of 60. Step sizes of L_{step} = 0.2 or 1 μm were used, and as explained later, quantitative results are reported for a 1 μm step size. Samples were held in epoxy or bakelite for cross-section observation. Samples were cross-section polished by grinding down to the mid-plane, mechanically polishing with a progression of SiC paper (600 and 800), diamond suspension (6 μm and 3 μm), 1 μm alumina suspension (10 min), and then 0.04 μm colloidal silica on a precision Multi-Prep semiautomatic polisher (Allied High Tech, 15 min). EBSD scan regions were chosen by best avoiding rare polishing scratches that could be observed in SEM secondary images. Spatial resolution at these conditions for Ta was found to be <70 nm horizontal and <140 nm vertical, determined by observation of changing Kikuchi pattern zone axes when moving horizontally or vertically across a grain boundary. The effects of tilt and alignment were found to shift repeated GND dislocation density results by only 20% by positioning the sample in grossly off-plane (~5°) loading conditions. Image drift was minimized during the scans by fully painting the epoxy or bakelite surfaces in conductive silver paste and also allowing for the SEM electron image to equilibrate for 5 min before starting an EBSD scan. Image drift was checked by comparing pre- and post- scan sample positions. In a worst-case-scenario where image drift was observed to be 0.15 μm/min diagonally during a 28 minute scan, the GND dislocation density dropped 35%, which is similar to location-to-location variation within one sample. Image drift was typically over an order of magnitude lower than this worst case, and scans that had drift approaching 0.1 μm/min in magnitude were thrown out.

Typically >99% of points in the Ta area were indexed. Band contrast (*BC*) is a measure of Kikuchi image quality at each step of an EBSD map and measured on a 0–255 scale. Mean angular deviation (*MAD*) is a measure of how well the Aztec software could index the Kikuchi pattern at each step. There was a trend for slightly higher *BC* and lower *MAD* on annealed samples, as might be expected. Annealed Starck Ta had $\langle BC \rangle = 150$ and $\langle MAD \rangle = 0.29°$, whereas coined Starck Ta had $\langle BC \rangle = 142$ and $\langle MAD \rangle = 0.44°$.

3.3. Solution algorithm: OpenXY

OpenXY [65] is a custom open-access Matlab-based environment for post-processing an EBSD scan dataset of Kikuchi diffraction pattern images. It has been validated with simulated and real dislocation structures [11,13,33] and used in various experimental studies [8,66,67].

Knowledge of the EBSD scan geometry is required for OpenXY analysis. Using our camera's Kikuchi image pixel aspect ratio of $V = 480/640 = 0.75$, OpenXY scan geometry coordinates (X^*, Y^*, Z^*) are automatically converted from Aztec's pattern center coordinates (PC_x, PC_y) and detector distance (DD) as: $X^* = PC_x/V - 1/(2V) + 1/2$, $Y^* = PC_y/V$, $Z^* = DD/V$. Typical geometry values were $X^* = 0.50$, $Y^* = 0.75$, and $Z^* = 0.65$. Dislocation density results proved insensitive to these pattern center coordinates, with only ~10% changes to large (±0.2) changes in these scaled coordinate inputs. Typical geometry estimates are assumed to be better than 0.1, hence the geometry estimates were deemed to be adequate [60].

The following OpenXY settings were used in the version downloaded July 15, 2016. Microscope settings were 20 keV, 70° sample tilt,

10° camera elevation, and 58 μm/pixel screen size. In Advanced Settings, a Real Grain Reference pattern with $IQ > Fit > CI$ was chosen along with a misorientation tolerance up to 10° and a ROI shift magnitude ($|\mathbf{q}|$) cut-off of two standard deviations away from the mean shift. In some scans, the step size was artificially increased by skipping pixels using OpenXY's built-in option, however most mapping and analysis was performed with a 1 μm step size. The OpenXY algorithm removed grain boundaries and low image quality regions from calculation. A 5–25° range of maximum misorientation tolerance was tested when indicated. Default OpenXY ROI and filter settings were used. The curl of a tensor is defined as in Ref. [11] and used consistently [16].

OpenXY includes three algorithms to solve for three different scalar GND dislocation densities: α_3, α_5, and α_9, where the subscript indicates the number of terms solved for in the Nye tensor. On both cold-worked and annealed test samples, results for α_3 and α_5 were within $\pm 10\%$ of each other and on average ~10% greater than α_9. These variations are on the order of variability over one annealed sample ($\pm 30\%$) and much smaller than the uncertainty we expect from ignoring SSD content. When comparing to total dislocation density measures (e.g. from microhardness) factor of two error bars in $\langle \rho_{GND} \rangle$ are assumed from the neglect of SSD dislocations in HR-EBSD; this also roughly corresponds to the standard deviation of the GND distribution over a whole map. Our maps are plotted using α_3. More detail can be found in Ref. [43] and the OpenXY application notes.

3.4. Microhardness procedure

Mircohardness readings were taken on polished flats with a Vickers tip using the Shimadzu HMV-G (Newage Testing Instruments) loaded for 15 s at 40× magnification. Samples were >10× thicker than indentation depths and indentations were >3 diameters from each other. Microhardness readings are from 2-axis fits and reported values are averaged over >3 different measurements with errors indicated by standard deviation. Two hardness standards were used to verify calibration: 246 ± 11 *HV* (Ellis 12267) and 422 ± 9 *HV* (Wilson 9ES). Microhardness values can depend on indent load, increasing both at small loads when size-dependent plasticity occurs [68], and at large loads when the bulk Hall-Petch grain-size effect occurs. We took readings at loads from 10 g to 500 g. The minimum microhardness reading was generally observed at 100–200 g and is assumed here to correspond to metal deformation without size-dependent or Hall-Petch effects. Microhardness texture variations are not considered and are assumed to be a significant contribution to the microhardness measurement error bars. Dislocation density estimates are extracted from these minimum Ta hardness measurements using the phenomenological relation derived previously [69], using assumptions for the flow stress Y of $Y = HV/3$ and $Y = 0.4Gb\sqrt{\rho_d}$ so that: $\rho_{d,\,HV} = 1.6 \times 10^9([9.8HV - 660]/\text{MPa})^2\ \text{m}^{-2}$, where 660 MPa is the ingot hardness of annealed Ta and the 9.8 factor converts *HV* values to MPa units.

4. Results and discussion

Fig. 2(a) shows the HR-EBSD measure of GND dislocation density variation with EBSD step size (L_{step}) in two different samples (each scanned in two locations) of both coined and annealed Starck Ta. Each scan is positioned in a small region of interest (8–40 μm in size) where we expect an average GND measurement to be reproducible. Specifically, in the case for microcoined Ta, we look at a region within ~λ below the ripple surface. Scans are taken at either $L_{step} = 0.2$ or 1 μm and higher effective step sizes are analyzed artificially by skipping neighbors in OpenXY analysis.

It is known the calculated ρ_{GND} from HR-EBSD depends on the step size used in the EBSD scan [9,13,14,36,43,70–72]. Using the continuous theory of dislocations model for analysis requires many more than one threaded dislocation contributing to lattice mismatch in the scan plane per EBSD step to avoid noise, and simultaneously much less than L_{step}/b GND dislocations per step due to the discrete nature of a lattice (if more, the Burgers circuit would not close within one EBSD step). Another interpretation of the ρ_{GND} upper limit is that the step size would be much larger than the anticipated scale of curvature changes [9]. These forbidden regions of analysis are indicated by dark shading in Fig. 2(a). In practice, the noise floor is more stringent than one dislocation per step, determined to be $\sim \Delta\theta_{min}/(Lb)$ where $\Delta\theta_{min}$ is the misorientation resolution of the HR-EBSD scan and image analysis [14,73]. The noise floor of HR-EBSD has been evaluated experimentally by scanning single crystal Si using the assumption that its actual dislocation density ($\sim 10^8$ m^{-2}) is much smaller than can be calculated by HR-EBSD [71]. Two similar control scans on single crystal Si wafers were performed here with results plotted in Fig. 2(a) as the noise limit and the noise-dominated region shaded in light gray. Our system's noise limit as a function of L_{step} was found to be very similar to that found in Ref. [71] and lower than any Ta sample analyzed.

Analysis of the microcoined Ta samples at variable step size in Fig. 2(a) indicates that there is a plateau in GND density in the $L_{step} = 1-4$ μm range. Although there may be a small shift near $L_{step} = 3$ μm, no obvious plateau is observed for annealed Ta. Similar trends have been seen previously in cold worked and annealed samples and simulations [13]. As previous work that suggests, $L_{step} = 1-3$ μm step would work for expected $\rho_{GND} = 10^{13} - 10^{15}\ \text{m}^{-2}$ [9,13]. Consequently, we choose $L_{step} = 1$ μm for further analysis and maps for the following reasons: the observation of the GND plateau, the optimization of EBSD scan time per map, the use of the same step size for all samples, and the observation of resolved dislocation structures. For example, Fig. 2(b) shows GND maps in small regions of both annealed and microcoined Ta. Note that as well as the average level decreasing with L_{step}, the dislocation structures can appear noisy at low step size or washed out at large step size. The choice of $L_{step} = 1$ μm for analysis of samples with $\rho_{GND} = 10^{13} - 10^{15}\ \text{m}^{-2}$ amounts to a rule of thumb of using 10–1000 GND dislocations per Burgers circuit for a continuum view.

The dislocation generation from microcoining can be seen in Fig. 3(a) maps, which compares ρ_{GND} for two separate foils of annealed 0.1 mm-thick Starck Ta before coining and after coining with an $A = 5$ μm, $\lambda = 50$ μm die pattern. As an aside, we also show some example Kikuchi patterns and cross-correlation **q** shift vector fields in Fig. 3(b) from the points indicated by "1", "2". and "3" in Fig. 3(a). These highlight data quality and how HR-EBSD calculations differ throughout the range of dislocation densities we study, e.g. $\sim 10^{13} - 10^{15}\ \text{m}^{-2}$. Note that these **q** shift vectors are used to calculate α_{ij} components for each Kikuchi pattern step and that they range from sub-pixel to a few pixels in these samples.

For the coined ripple that forms as if effectively in a closed die [41] we see a ~10× amplification of GND on average in the ripple region. This ~10× amplification appears relatively uniform in a region ~λ deep under the ripple surface. The absolute value of $\langle \rho_{GND} \rangle = 3 \times 10^{14}$ m^{-2} is in range of that predicted by a simple strain gradient plasticity approximation and an effective plastic strain of $\bar{\varepsilon} = 0.5$ [41] (as discussed above). However, in this case where a single grain encompasses most of the coined ripple, we also see significant non-uniform GND accumulation after coining, with ~100× amplification in four bands of pile ups that radiate approximately from the ripple peak (right side of Fig. 3(a) and also in (d)). Note that some of the dislocation content in these bands results in a local misorientation higher than the OpenXY HR-EBSD algorithm was programmed to account for (10° over a 1 μm step). We will return to this below. We hypothesize these high-GND bands correspond to the migrating centered fan borders in the non-stationary slip line field for coining. It is interesting that the GND bands appear affected by grain boundaries. Note that the upper band (con-

taining spot "3" in Fig. 3(a)) looks to stop as it connects to a grain boundary within the metal.

Fig. 3(c) shows more maps of the annealed and microcoined Ta samples. Inverse pole figures (IPF) in the sample normal direction (horizontal in map) and kernel average misorientation (KAM) are provided using the Aztec software Hough orientation data, and GND maps are provided using the Open XY HR-EBSD data. Moving left to right on the first three maps of Fig. 3(c), we gain increasing amount of information on the deformation of the coined microripple. The coined Ta IPF map indicates local texture variations exist in a coined surface grain. The coined Ta KAM map indicates some misorientation banding, however the resolution is limited to ~10× differences in misorientation due to the use of Hough transform image analysis, where misorientations $<0.6^{\circ}$ are indistinguishable from noise. However, the HR-EBSD GND map provides quantitative measurements of GND dislocation density that capture >100× variations. Furthermore, the HR-EBSD data can be decomposed into α_{ij} components (where OpenXY defines the 1–2 plane as the observed cross-section and the 3 direction is out of the page). Note that the prominent bands have strong α_{13} and α_{23} signatures, indicative of the expected plane strain of the ripple geometry. Fig. 3(d) is a different representation of the coined Ta KAM map where orientation boundaries $2-10^{\circ}$ are plotted in red and $>10^{\circ}$ are plotted in black. The multiple parallel $2-10^{\circ}$ boundaries again highlight the organized dislocation wall formation within a surface grain. We hypothesize that since Ta is a bcc material with many available slip systems, this geometry of banding is relatively insensitive to the deformed grain texture.

Fig. 3(d) show three different OpenXY HR-EBSD maps for the coined Ta sample using increasing maximum misorientation values between pixels ($5^{\circ}-25^{\circ}$). We see little difference between the maximum misorientation 10° and 25° maps, and both indicate there are narrow bands where the lattice rotation changes dramatically over one pixel within the surface grain. A boundary of rapid, large change in lattice rotation was also previously seen in HR-EBSD of a sharp right-angle wedge indenter [9]. Note that equating the elastic and plastic incompatibilities due to dislocations in the HR-EBSD analysis is based on small deformation theory, so HR-EBSD analysis of large local rotations, e.g. $>10^{\circ}$, would require a further approximation that a small angle linearization holds at high misorientations. For HR-EBSD to quantify ρ_{GND} in the narrow regions of these bands that are currently ignored in OpenXY, a smaller step size (estimated <250 nm) would be required.

Fig. 4 shows deformation maps in different regions of the same coined sample, centered either in a ripple peak, (Fig. 4(a)), under a ripple valley (Fig. 4(b)), and 40 ± 10 μm below the coined surface (Fig. 4(c)). Additionally we plot the GND dislocation density scaled by the average in the pre-coined annealed Ta, $\langle\rho_{GND,\,0}\rangle = 2\times10^{13}$ m^{-2}. The average was taken over whole field of the raw material averaged in 5 single grain scans and 2 scans with 10–30 grains. The two ripple region scans show up to ~100× inhomogeneous GND amplification, and results indicate complex interplay between bands and grain boundaries. In the scan centered at a ripple valley (Fig. 4(b)), indications of the dislocation banding can be seen in the neighboring ripple peaks, however the many grain boundaries pre-existing there appear to disrupt the band patterning. As predicted by microcoining forming modeling [41] and as suggested by the extreme left (internal) region of our initial GND map of the coined Ta (Fig. 3(a)), the amplified dislocation density is likely mostly confined near the surface in a layer of ~λ deep. The additional scan (Fig. 4(c)) centered 40 ± 10 μm deep in from the ripple midplane indicates the presence of an elastic-plastic boundary since the GND density drastically drops to levels near the starting annealed material at a distance ~λ below the coining surface. The elastic-plastic boundary also appears closely linked to the grain boundaries, which in this case nearly divides the elastic and plastic regions of deformation. Finally, qualitatively comparing these to previous HR-EBSD of fcc Ni [30], GNDs are not as prominently stacked at grain boundaries in this bcc material. This might be expected due to Ta's very high stacking fault energy that would preferentially lead to cross-slip over grain boundary stacking [3].

These dislocation maps can be positioned in locations where centered fans are expected to reside in the coining slip line field to evaluate the expected $1/r^2$ radial distribution of GND dislocation density from the fan center. Fig. 5 shows the GND dislocation density variations moving into the coined surface along radial lineouts extending from assumed final positions of the coining slip line field centered fans for two different regions: the edges of the coining die in an open die configuration (Fig. 5(a)) and at a ripple peak in an effectively closed die configuration (Fig. 5(b)). The $r = 0$ location corresponds to the surface of the Ta at the edge of the die contact in Fig. 5(a) and on the ripple peak in Fig. 5(b). Note that the orientation analysis in Fig. 5(a) is performed with OpenXY Hough algorithm since these scans only had Aztec orientation data without the saved Kikuchi pattern dataset. Considering the high ρ_{GND} values in this scan, we don't expect large differences in the Hough and cross-correlation results. For example, a previous comparison for a fcc indentation showed a systematic ~40% shift to higher GND values obtained from the Hough algorithm [15]. In both regions investigated, ρ_{GND} falls as $\sim r^{-1.3}$ averaged over all data. Though there are several simplifications in the slip line prediction and we expect more samples would be needed to test the exact power law exponent, these trends of dislocation fall off support the notion of localized dislocation generation by slip along curved slip lines in this bcc material. However, note the differences in the uniformity by rotating through the fan regions at constant r. The GND density is relatively uniform at constant r in the large-scale fan, whereas it is non-uniform with cell walls in small-scale single grain fan.

From our various Ta dislocation density maps, we saw indications that an average GND density would be reproducible in some regions of interest large enough to obtain a microhardness measurement (from indents of ~15–40 μm diagonal size). These regions correspond to anywhere in the bulk of an annealed or cold-rolled foil and the surface region (~λ-deep) of a coined foil. Dislocation density can be extracted from both HR-EBSD and microhardness using two different mechanical models, one based on deformation compatibility and one for flow stress. As long as the HR-EBSD measure is averaged over a region comparable to the microhardness indent, we would expect $\langle\rho_{GND}\rangle$ as a lower-bound for $\rho_{d,\,HV}$. Consequently we were able to compare HR-EBSD measurements of $\langle\rho_{GND}\rangle$ (at $L_{step} = 1$ μm) to corresponding $\rho_{d,\,HV}$ estimates from microhardness using the method indicated in the Experimental section. Fig. 6(a) shows $\langle\rho_{GND}\rangle$ vs. $\rho_{d,\,HV}$ for regions of Ta samples with very different deformation history, from annealed to cold-worked with dislocation densities varying from 10^{13} to 10^{15} m^{-2}. Sample microhardness measurements as a function of load are provided in Fig. 6(b), where minimum values (HV_{min}) are used to generate Fig. 6(a). A hypothetical perfect match in Fig. 6(a) is indicated by the solid line. We found $\langle\rho_{GND}\rangle$ a factor of 1–2 lower than $\rho_{d,\,HV}$ obtained from HV measurements over the two orders of magnitude of $\rho_{d,\,HV}$ examined. We see somewhat better validation of cold worked samples with $\langle\rho_{GND}\rangle > 10^{14}$ m^{-2} as might be expected since the ratio of GND/SSD dislocations would be higher and there is less uncertainty from the 1 μm HR-EBSD step size choice. We also see HR-EBSD data begin to flatten at the lowest values near 10^{13} m^{-2}, presumably due to approach to our system's HR-EBSD noise limit.

5. Conclusions

We used HR-EBSD to map dislocation density in microcoined rippled Ta foils. We found:

- A ~10× GND dislocation density amplification compared to the raw material in a ripple wavelength-deep surface region with a ~100× amplification in bands that radiate from the surface.
- The GND dislocation density drops when moving into the coined metal along expected central fan slip lines. This effect is explained by an approximation from slip line fields and was observed on both the large-scale edges of die compression and the small scale of a single extruded ripple.
- Average HR-EBSD GND dislocation densities were corroborated as a lower bound for total dislocation density from microhardness measurements and an indentation model. Values of ρ_{GND} from HR-EBSD were a factor of $1-2\times$ lower than $\rho_{d,HV}$ from microhardness in tantalum samples of varied deformation (for $\rho_d = 10^{13}-10^{14}$ m^{-2} annealed and $\rho_d = 10^{14}-10^{15}$ m^{-2} cold worked tantalum).

Comparisons between lower-bound dislocation densities from HR-EBSD and other measurements (e.g. TEM) are suggested in the future for other materials and applications. Furthermore, adding analysis to delineate the missing SSD content in HR-EBSD may improve agreement [13,34].

It is interesting that arguments from slip line fields that assume many slip systems can be used to reconcile some of the dislocation structures observed on a single grain scale in this bcc material. However, we observed that grain boundaries can distort these structures. An expanded follow up study with fcc and hcp metals and comparisons between single crystal and polycrystalline cases is expected to exhibit texture-controlled and scale-dependent dislocation structures in the microformed surface.

Declarations of interest

None.

Acknowledgements

Work at General Atomics was funded by General Atomics Internal Research and Development and the Department of Energy Science Undergraduate Laboratory Internship (SULI). The BYU team was supported by U.S. Department of Energy (DOE), Office of Science, Basic Energy Sciences (BES), under award No. DE-SC0012587. We thank Don Wall, Brian Stahl, and Emily Mathison for SEM work and Jack Knipping and Lorenzo Inandan for polishing. We thank the reviewers for comments that helped improve the paper.

Data availability

EBSD scan data and Kikuchi pattern images for our primary maps are uploaded on Google Drive link: https://drive.google.com/drive/folders/1rjNx5avBb24QRnn4NO2Kz5xFao-Mbna_?usp=sharing.

References

[1] D. Hull, D.J. Bacon, Introduction to Dislocations, Great Britain, Elsevier, 2011.
[2] U.F. Kocks, A.S. Argon, M.F. Ashby, Thermodynamics and Kinetics of Slip, Pergamon Press, Oxford, 1975.
[3] M.A. Meyers, K.K. Chawla, Mechanical Metallurgy, Prentice-Hall, New Jersey, 1984.
[4] A. Arsenlis, D. Parks, Crystallographic aspects of geometrically-necessary and statistically-stored dislocation density, Acta Mater. 47 (5) (1999) 1597–1611.
[5] U. Engel, R. Eckstein, Microforming - from basic research to its realization, J. Mater. Process. Technol. 233-236 (2003) 449–456.
[6] T. Britton, H. Liang, F. Dunne, A. Wilkinson, The effect of crystal orientation on the indentation response of commercially pure titanium: experiments and simulations, Proc. R. Soc. London, Ser. A 466 (2010) 695–719.
[7] E. Demir, D. Raabe, N. Zaafarani, S. Zaefferer, Investigation of the indentation size effect through the measurement of the geometrically necessary dislocations beneath small indents of different depths using EBSD tomography, Acta Mater. 57 (2) (2009) 559–569.
[8] B.E. Dunlap, T.J. Ruggles, D.T. Fullwood, B. Jackson, M.A. Crimp, Comparison of dislocation characterization by electron channeling contrast imaging and cross-correlation electron backscattered diffraction, Ultramicroscopy 184 (2018) 125–133.
[9] J. Kysar, Y. Saito, M. Oztop, D. Lee, W. Huh, Experimental lower bounds on geometrically necessary dislocation density, Int. J. Plast. 26 (8) (2010) 1097–1123.
[10] J.W. Kysar, Y.X. Gan, T.L. Morse, X. Chen, M.E. Jones, High strain gradient plasticity associated with wedge indentation into face-centered cubic single crystals: geometrically necessary dislocation densities, J. Mech. Phys. Solids 55 (7) (2007) 1554–1573.
[11] T. Ruggles, D. Fullwood, Estimations of bulk geometrically necessary dislocation density using high resolution EBSD, Ultramicroscopy 133 (2013) 8–15.
[12] T. Ruggles, D. Fullwood, J. Kysar, Resolving geometrically necessary dislocation density onto individual dislocation types using EBSD-based continuum dislocation microscopy, Int. J. Plast. 76 (2016) 231–243.
[13] T. Ruggles, T. Rampton, A. Khosravani, D. Fullwood, The effect of length scale on the determination of geometrically necessary dislocations via EBSD continuum dislocation microscopy, Ultramicroscopy 164 (2016) 1–10.
[14] A.J. Wilkinson, D. Randman, Determination of elastic strain fields and geometrically necessary dislocation distributions near nanoindents using electron back scatter diffraction, Philos. Mag. 90 (9) (2010) 1159–1177.
[15] T.B. Britton, J.L.R. Hickey, Understanding deformation with high angular resolution electron backscatter diffraction (HR-EBSD), In: IOP Conference Series: Materials Science and Engineering, vol. 304, IOP Publishing, 2018, p. 012003.
[16] S. Das, F. Hofmann, E. Tarleton, Consistent determination of geometrically necessary dislocation density from simulations and experiments, Int. J. Plast. 109 (2018) 18–42.
[17] B.A. Remington, R.E. Rudd, J.S. Wark, From microjoules to megajoules and kilobars to gigabars: probing matter at extreme states of deformation, Phys. Plasmas 22 (9) (2015), 090501.
[18] N. Barton, J. Bernier, R. Becker, A. Arsenlis, R. Cavallo, J. Marian, M. Rhee, H.-S. Park, B. Remington, R. Olson, A multiscale strength model for extreme loading conditions, J. Appl. Phys. 109 (7) (2011), 073501.
[19] R.E. Rudd, H.-S. Park, R. Cavallo, A. Arsenlis, D. Orlikowski, S. Prisbrey, C. Wehrenberg, B. Remington, Modeling of grain size strengthening in tantalum at high pressures and strain rates, In: AIP Conference Proceedings, vol. 1793, AIP Publishing, 2017, p. 110004.
[20] H.-S. Park, R. Rudd, R. Cavallo, N. Barton, A. Arsenlis, J. Belof, K. Blobaum, B. El-Dasher, J. Florando, C. Huntington, et al., Grain-size-independent plastic flow at ultrahigh pressures and strain rates, Phys. Rev. Lett. 114 (6) (2015), 065502.
[21] P. Morin, M. Pitaval, D. Besnard, G. Fontaine, Electron–channelling imaging in scanning electron microscopy, Philos. Mag. A 40 (4) (1979) 511–524.
[22] S. Zaefferer, N.-N. Elhami, Theory and application of electron channelling contrast imaging under controlled diffraction conditions, Acta Mater. 75 (2014) 20–50.
[23] B. El-Dasher, B. Adams, A. Rollett, Viewpoint: experimental recovery of geometrically necessary dislocation density in polycrystals, Scr. Mater. 48 (2) (2003) 141–145.
[24] C.J. Gardner, B.L. Adams, J. Basinger, D.T. Fullwood, EBSD-based continuum dislocation microscopy, Int. J. Plast. 26 (8) (2010) 1234–1247.
[25] V. Randle, N. Hansen, D.J. Jensen, The deformation behaviour of grain boundary regions in polycrystalline aluminium, Philos. Mag. A 73 (2) (1996) 265–282.
[26] S. Sun, B. Adams, W. King, Observations of lattice curvature near the interface of a deformed aluminium bicrystal, Philos. Mag. A 80 (1) (2000) 9–25.
[27] S.I. Wright, M.M. Nowell, D.P. Field, A review of strain analysis using electron backscatter diffraction, Microsc. Microanal. 17 (03) (2011) 316–329.
[28] M. Ashby, The deformation of plastically non-homogeneous materials, Philos. Mag. 21 (170) (1970) 399–424.
[29] A.J. Wilkinson, G. Meaden, D.J. Dingley, High-resolution elastic strain measurement from electron backscatter diffraction patterns: new levels of sensitivity, Ultramicroscopy 106 (4) (2006) 307–313.
[30] C. Wang, C. Wang, J. Xu, P. Zhang, D. Shan, B. Guo, Interactive effect of microstructure and cavity dimension on filling behavior in microcoining of pure nickel, Sci. Rep. 6 (2016), 23895.
[31] N. Fleck, G. Muller, M. Ashby, J. Hutchinson, Strain gradient plasticity: theory and experiment, Acta Metall. Mater. 42 (2) (1994) 475–487.
[32] J. Jiang, T.B. Britton, A.J. Wilkinson, Evolution of intragranular stresses and dislocation densities during cyclic deformation of polycrystalline copper, Acta Mater. 94 (2015) 193–204.
[33] L.T. Hansen, B.E. Jackson, D.T. Fullwood, S.I. Wright, M. De Graef, E.R. Homer, R.H. Wagoner, Influence of noise-generating factors on cross-correlation electron backscatter diffraction (EBSD) measurement of geometrically necessary dislocations (GNDs), Microsc. Microanal. 23 (3) (2017) 460–471.
[34] A.J. Wilkinson, E. Tarleton, A. Vilalta-Clemente, J. Jiang, T.B. Britton, D.M. Collins, Measurement of probability distributions for internal stresses in dislocated crystals, Appl. Phys. Lett. 105 (18) (2014), 181907.
[35] D. Field, C. Merriman, N. Allain-Bonasso, F. Wagner, Quantification of dislocation structure heterogeneity in deformed polycrystals by EBSD, Model. Simul. Mater. Sci. Eng. 20 (2) (2012), 024007.
[36] P.J. Konijnenberg, S. Zaefferer, D. Raabe, Assessment of geometrically necessary dislocation levels derived by 3d EBSD, Acta Mater. 99 (2015) 402–414.
[37] F. Ram, Z. Li, S. Zaefferer, S.M.H. Haghighat, Z. Zhu, D. Raabe, R.C. Reed, On the origin of creep dislocations in a Ni-base, single-crystal superalloy: an ECCI, EBSD, and dislocation dynamics-based study, Acta Mater. 109 (2016) 151–161.
[38] J. Seal, T. Bieler, M. Crimp, B. Britton, A. Wilkinson, Characterizing slip transfer in commercially pure titanium using high resolution electron backscatter diffraction (HR-EBSD) and electron channeling contrast imaging (ECCI), Microsc. Microanal. 18 (S2) (2012) 702–703.
[39] A. Vilalta-Clemente, G. Naresh-Kumar, M. Nouf-Allehiani, P. Gamarra, M. di Forte-Poisson, C. Trager-Cowan, A. Wilkinson, Cross-correlation based high resolu-

strain mapping and dislocation distributions in InAlN thin films, Acta Mater..125 (2017) 125–135.
[40] G.C. Randall, J. Vecchio, J. Knipping, D. Wall, T. Remington, P. Fitzsimmons, M. Vu, E.M. Giraldez, B.E. Blue, M. Farrell, A. Nikroo, Developments in microcoining rippled metal foils, J. Fus. Sci. Tech. 63 (2013) 274–281.
[41] G.C. Randall, J. Dahal, J. Vecchio, S. Agarwal, R. Mehta, G. Ravichandran, A. Stebner, Microcoining ripples in metal foils, Int. J. Mech. Sci. 148 (2018) 263–271.
[42] N. Bay, T. Wanheim, Real area of contact between a rough tool and a smooth workpiece at high normal pressure, Wear 38 (1976) 225–234.
[43] T. Ruggles, Characterization of Geometrically Necessary Dislocation Content With EBSD-based Continuum Dislocation Microscopy, Ph.D. thesis Brigham Young University-Provo, 2015.
[44] A. Wilkinson, E. Clarke, T. Britton, P. Littlewood, P. Karamched, High-resolution electron backscatter diffraction: an emerging tool for studying local deformation, J. Strain Anal. Eng. 45 (5) (2010) 365–376.
[45] P. Cermelli, M.E. Gurtin, On the characterization of geometrically necessary dislocations in finite plasticity, J. Mech. Phys. Solids 49 (7) (2001) 1539–1568.
[46] B. Bilby, R. Bullough, E. Smith, Continuous distributions of dislocations: a new application of the methods of non-Riemannian geometry, Proc. R. Soc. London, Ser. A 231 (1955) 263–273.
[47] I. Groma, Statistical physical approach to describe the collective properties of dislocations, In: Multiscale Modelling of Plasticity and Fracture by Means of Dislocation Mechanics, Springer, 2010, pp. 213–270.
[48] E. Kröner, General continuum theory of dislocations and proper stresses, Arch. Ration. Mech. Anal. (1960) 273–334.
[49] E. Kröner, Benefits and shortcomings of the continuous theory of dislocations, Int. J. Solids Struct. 38 (6) (2001) 1115–1134.
[50] J. Nye, Some geometrical relations in dislocated crystals, Acta Metall. 1 (2) (1953) 153–162.
[51] D. Dingley, Progressive steps in the development of electron backscatter diffraction and orientation imaging microscopy, J. Microsc. 213 (3) (2004) 214–224.
[52] O. Engler, V. Randle, Introduction to Texture Analysis, CRC Press, Boca Raton, FL, 2010.
[53] F. Humphreys, Review grain and subgrain characterisation by electron backscatter diffraction, J. Mater. Sci. 36 (16) (2001) 3833–3854.
[54] A.J. Wilkinson, T.B. Britton, Strains, planes, and EBSD in materials science, Mater. Today 15 (9) (2012) 366–376.
[55] S. Zaefferer, On the formation mechanisms, spatial resolution and intensity of backscatter Kikuchi patterns, Ultramicroscopy 107 (2) (2007) 254–266.
[56] W. Pantleon, Resolving the geometrically necessary dislocation content by conventional electron backscattering diffraction, Scr. Mater. 58 (11) (2008) 994–997.
[57] T. Britton, A. Wilkinson, High resolution electron backscatter diffraction measurements of elastic strain variations in the presence of larger lattice rotations, Ultramicroscopy 114 (2012) 82–95.
[58] J. Kacher, C. Landon, B.L. Adams, D. Fullwood, Bragg's law diffraction simulations for electron backscatter diffraction analysis, Ultramicroscopy 109 (9) (2009) 1148–1156.
[59] A.J. Wilkinson, G. Meaden, D.J. Dingley, High resolution mapping of strains and rotations using electron backscatter diffraction, Mater. Sci. Technol. 22 (11) (2006) 1271–1278.
[60] T. Britton, C. Maurice, R. Fortunier, J.H. Driver, A. Day, G. Meaden, D. Dingley, K. Mingard, A. Wilkinson, Factors affecting the accuracy of high resolution electron backscatter diffraction when using simulated patterns, Ultramicroscopy 110 (12) (2010) 1443–1453.
[61] L. Kubin, A. Mortensen, Geometrically necessary dislocations and strain-gradient plasticity: a few critical issues, Scr. Mater. 48 (2) (2003) 119–125.
[62] N. Fleck, M. Ashby, J. Hutchinson, The role of geometrically necessary dislocations in giving material strengthening, Scr. Mater. 48 (2) (2003) 179–183.
[63] W.F. Hosford, R.M. Caddell, Metal Forming: Mechanics and Metallurgy, Cambridge University Press, Cambridge, UK, 2011.
[64] G. Regazzoni, A.L. Douaron, F. Montheillet, A new method for the analysis of a non-stationary two-dimensional flow and its application to the closed-die forging of a rib, J. Mech. Work. Technol. 5 (1981) 281–296.
[65] OpenXY, in: https://github.com/BYU-MicrostructureOfMaterials/OpenXY, Accessed 15 July 2016.
[66] M. Bird, T. Rampton, D. Fullwood, P. Becher, K. White, Local dislocation creep accommodation of a zirconium diboride silicon carbide composite, Acta Mater. 84 (2015) 359–367.
[67] A. Khosravani, D. Fullwood, B. Adams, T. Rampton, M. Miles, R. Mishra, Nucleation and propagation of twins in AZ31 magnesium alloy, Acta Mater. 100 (2015) 202–214.
[68] N. Stelmashenko, M. Walls, L. Brown, Y.V. Milman, Microindentations on W and Mo oriented single crystals: an STM study, Acta Metall. Mater. 41 (10) (1993) 2855–2865.
[69] H. Stüwe, A. Padilha, F. Siciliano Jr, Competition between recovery and recrystallization, Mater. Sci. Eng. A 333 (1–2) (2002) 361–367.
[70] B.L. Adams, C.J. Gardner, D.T. Fullwood, EBSD-based dislocation microscopy, In: Solid State Phenomena, Trans Tech Publ, vol. 160, 2010, pp. 3–10.
[71] J. Jiang, T. Britton, A. Wilkinson, Measurement of geometrically necessary dislocation density with high resolution electron backscatter diffraction: effects of detector binning and step size, Ultramicroscopy 125 (2013) 1–9.
[72] M. Kamaya, Assessment of local deformation using EBSD: quantification of accuracy of measurement and definition of local gradient, Ultramicroscopy 111 (8) (2011) 1189–1199.
[73] P. Littlewood, T. Britton, A. Wilkinson, Geometrically necessary dislocation density distributions in Ti–6Al–4V deformed in tension, Acta Mater. 59 (16) (2011) 6489–6500.